

Supplementary Information

Development of a Mechanically Flexible 2D-MXene Membrane Cathode for Selective Electrochemical Reduction of Nitrate to N₂: Mechanisms and Implications

Yang Li[†], Jinxing Ma[‡], T. David Waite[‡], Michael R. Hoffmann[§], Zhiwei Wang^{†*}

¹ State Key Laboratory of Pollution Control and Resource Reuse, Shanghai Institute of Pollution Control and Ecological Security, School of Environmental Science and Engineering, Tongji University, 1239 Siping Road, Shanghai 200092, China

² School of Civil and Environmental Engineering, The University of New South Wales, Sydney, New South Wales 2052, Australia

³ California Institute of Technology, The Linde-Robinson Laboratory, 1200 E. California Blvd., Pasadena, CA 91125, USA

Number of pages (including the cover page): 36

Number of figures: 36

Number of tables: 6

Contents

Text sections

Section S1. Diffusion behavior of nitrate in the cathode

Section S2. Physicochemical characterization.

Section S3. Permeability and porosity of membrane.

Section S4. Electrochemical performance measurements.

Section S5. Electrochemical nitrate reduction.

Section S6. DFT calculation.

Figures

Figure S1. Diffusion behavior of nitrate in the cathode surface.

Figure S2. AFM images of MXene nanosheets and ANF.

Figure S3. TEM images of MXene nanosheets.

Figure S4. Plots of displacement vs. load of MXene membrane for the indentation test.

Figure S5. Doppler broadening W parameter of $\text{Ti}_3\text{C}_2\text{T}_x$ MXene and Ti_3AlC_2 .

Figure S6. Doppler broadening W-S parameters of $\text{Ti}_3\text{C}_2\text{T}_x$ MXene and Ti_3AlC_2 .

Figure S7. Schematic illustration of the H-shaped electrochemical cell.

Figure S8. Effects of variation in potential on pollutant removal.

Figure S9. Kinetics of the electrochemical NO_3^- reduction.

Figure S10. Areal capacitance of the MXene membrane.

Figure S11. Products of nitrate reduction under different Na^+ and Ca^{2+} concentration.

Figure S12. Detection of electrochemically active surface area.

Figure S13. The potential of zero charge for the MXene membrane.

Figure S14. The removal efficiency of NaNO_3 , KNO_3 , and $\text{Ca}(\text{NO}_3)_2$.

Figure S15. Schematic illustration of the continuous-flow device.

Figure S16. Proposed reaction pathway of nitrate electrochemical reduction on the defect-free MXene sites.

Figure S17. SEM images of cross-section of the MXene membrane.

Figure S18. XPS of MXene membrane before and after electrochemical nitrate reduction.

Figure S19. O 1s spectra of the as-prepared MXene membrane.

Figure S20. Zeta potential measurements.

Figure S21. Water contact angles measurements.

Figure S22. LSVs recorded in 10 mM Na₂SO₄ and 10 mM NaNO₃.

Figure S23. Peak heights on square root of scan rate measured by LSV.

Figure S24. EIS Nyquist plots of the MXene cathode.

Figure S25. Chronoamperometry experiments of MXene membrane at different potentials (vs Ag/AgCl).

Figure S26 Electrochemical reduction of low concentration nitrate under the flow-through filtration.

Figure S27 Cyclic voltammograms and calculated diffusion coefficient of nitrate.

Figure S28 Leaching of Ti of MXene membrane during the nitrate removal.

Figure S29 XRD patterns of the MXene membrane before and after the nitrate removal.

Figure S30 Calculated transition barrier energy profiles.

Figure S31 SAXS profiles of the MXene membrane.

Figure S32 Calculated free energy of the proposed reaction pathways.

Figure S33 The deformation charge density of *NO₃.

Figure S34 Calculated free energies of HER process.

Figure S35 Calculated adsorption energies of H₂ on the MXene

Figure S36 Effects of ORR process on pollutant removal.

Tables

Table S1. Polyethylene glycol (PEG) rejection by the MXene membrane.

Table S2. Nitrate rejection of the MXene membrane.

Table S3. The concentration of free chlorine at different applied potential.

Table S4. Comparison of the 2D-MXene electrochemical NO₃⁻ reduction performance to literature.

Table S5. The yield rate and Faradaic efficiency (FE) of H₂ in the electrochemical nitrate reduction.

Table S6. The yield rate and Faradaic efficiency (FE) of H₂ in Na₂SO₄ solution.

Section S1. Diffusion behaviour of nitrate in the cathode

The diffusion coefficient of NO_3^- to the cathode can be calculated according to the Randles-Sevcik equation¹:

$$I_p = (2.69 \times 10^5) \times Z^{3/2} \times A \times (D_{\text{NO}_3^-})^{1/2} \times \nu^{1/2} \times C_{\text{NO}_3^-} \quad (\text{S1})$$

where I_p is the peak current (A), Z is the number of reaction electron ($Z=1$), A is the effective area of the electrode ($A=2 \times 10^{-4} \text{ m}^2$), $D_{\text{NO}_3^-}$ is the diffusion coefficient of nitrate anion ($\text{m}^2 \text{ s}^{-1}$), ν is the scan rate (V s^{-1}), and $C_{\text{NO}_3^-}$ is the concentration of nitrate ($C_{\text{NO}_3^-} = 10 \text{ mol m}^{-3}$).

Herein, we used a common cathode (Cu electrode) to investigate the diffusion behaviour of nitrate under electrostatic repulsion. The CV curves of Cu at different scan rates are presented in Figure S1a, and the nitrate diffusion coefficients are shown in Figure S1b. The diffusion coefficients are substantially lower than the reported values in the absence of an electric field ($1.93 \times 10^{-9} \text{ m}^2 \text{ s}^{-1}$), revealing that the rate of transport of nitrate to the cathode is reduced as a result of electrostatic repulsion. As such, the adsorption of nitrate to the cathode active sites is substantially less favorable in the presence compared to the absence of an applied potential.

We then investigated the diffusion coefficients of nitrate in the MXene membrane under the flow-by and flow-through modes. In the flow-through mode, the CV curves are obtained at the flux of $100 \text{ L m}^{-2} \text{ h}^{-1}$. The relevant curves and calculated diffusion coefficients are presented in Figure S26. The diffusion coefficients of nitrate in the flow-by and flow-through modes are $2.04 \times 10^{-9} \text{ m}^2 \text{ s}^{-1}$ and $0.14 \times 10^{-9} \text{ m}^2 \text{ s}^{-1}$, respectively.

Section S2. Physicochemical characterization

Physical characterization of the MXene nanosheets and the MXene membrane includes the use of atomic force microscope, transmission electron microscopy, nanoindentation, positron annihilation spectroscopy, scanning electron microscopy, X-ray photoelectron spectroscopy, electrokinetic analyzer, water contact angle

detector, X-ray diffraction, small-angle X-ray scattering. The corresponding figures are provided in Figure S2, Figure S3, Figure S4, Figure S5, Figure S6, Figure S17, Figure S18, Figure S19, Figure S20, Figure S21, Figure S28, Figure S30.

The obtained $\text{Ti}_3\text{C}_2\text{T}_x$ nanosheets are around 5 nm thick and 200 nm in lateral size. The nanofibrils colloids have a high aspect ratio with a uniformly square cross-section of around 10 nm and length up to several hundred nm. The thickness of ANF is around 2 nm. Keithley SourceMeter 2400 was used to study the surface conductive properties of the investigated electro-devices. Two-point experiments were conducted by applying a voltage sweep from -6 to 6 V to study the conductive properties at the macroscopic level. The underlying structure inside the membrane is formed by stacking single-layer or a few-layer MXene nanosheets, and then by crosslinking different stacked layers by aramid fibers. The underlying structure inside the membrane is formed by stacking single-layers (or, at most, a few layers) of MXene nanosheets with the different layers cemented together by crosslinking with aramid fibers.

The mechanical flexibility and Young's modulus are crucial properties to evaluate the mechanical stability for a free-standing membrane.² The curly membrane is shown in Figure 1, suggesting a good mechanical flexibility of membrane. As shown in Figure S4, the Young's modulus can be conducted by the plot of displacement vs. load of MXene membrane, and the corresponding value is 1.4 Gpa.

The data in Figure S19 was obtained under two conditions: Na_2SO_4 at -0.8 V and NaNO_3 without applied potential. After the experiment, there is no significant change in the peaks assigned to oxygen vacancies under these conditions. Therefore, peak intensity changes should be attributed to nitrate adsorption and reduction.

The zeta potentials of pristine MXene, MXene membrane, and ANF membrane are -14.1 mV, -13.5 mV, -9.3 mV, respectively, at a neutral condition (Figure S20).

The hydrophilicities of pristine MXene, MXene membrane, and ANF membrane are illustrated in Figure S21. The water contact angles of pristine MXene (containing 0% ANF), MXene membrane, and ANF membrane (containing 100% ANF) are 21.36° , 52.82° , 60.46° , respectively.

The tortuosity (τ) is evaluated by the ratio of the total length of water transport (L) over the total distance in the vertical direction (H), *i.e.*, $\tau = L/H$, assuming the nanosheets are stacked in a perfect lamellar structure³. There are n layers of an average horizontal trajectory. The total path length and total vertical distance are $L = n(l+h)$ and $H = nh$, respectively, where l is the horizontal distance of nanosheets and h is the interlayer spacing of nanosheets traveled by a water molecule across a single layer ($L \approx nl$ as $l \gg h$). Because the membrane thickness is sufficiently large (10 μm). The average tortuosity is a constant value that can be defined as the average transport path across a single layer ($\tau = L/H \approx l/h$). In this work, the average horizontal distance that water travels in an MXene nanosheet is around 200 nm, whereas the interlayer spacing of nanosheets is 6.5 nm. Thus, the tortuosity is around 30.8 in the MXene membrane.

Section S3. Permeability and porosity of membrane

The membrane permeability is $\sim 250 \text{ L m}^{-2} \text{ h}^{-1} \text{ bar}$. The porosity of the obtained membrane was analyzed by mercury intrusion porosimeter (MIP, AutoPore IV 9500) and the corresponding porosity found to be 72%.

Section S4. Electrochemical performance measurements

Experiments were conducted in an H-shaped electrochemical cell which was equipped with a proton exchange membrane. An MXene membrane cut into an oblong film with an area of 2 cm^2 was used as the working electrode. Pt foil with the area of 1 cm^2 was used as the counter electrode while an Ag/AgCl electrode was used as the reference electrode. The electrode spacing for anode and cathode, anode and reference electrode, cathode and reference electrode is 1.0 cm. All experimental data was recorded using a potentiostat (CHI 660E). Galvanostatic charge-discharge (GCD) curves of Na^+ were obtained for the MXene membrane at a sodium concentration of 7.62 mM (equivalent to the sodium concentration in the continuous flow experiment). The results of the GCD curves and areal capacitance are provided in Figure S10. As

shown in Figure S10, the areal capacitance of the MXene membrane for Na⁺ was in the range of 50.3~22.6 mF cm⁻² at 1~10 mA cm⁻². As such, the impact of sodium intercalation on the electrochemical reduction of nitrate is insignificant under these conditions (please see Figure S11a). In previous work, most electrochemical capacitors can achieve an areal capacitance of > 350 mF cm⁻².^{4,5} Therefore, it is evident that the MXene membrane used in these studies possesses limited capacitive ability under the conditions used in these nitrate reduction studies.

To measure the electrochemically active surface area (ECSA), the electrochemical double-layer capacitance (C_{DL}) was first determined from the static CV. This range is typically a 0.1 V potential window centered at the open-circuit potential (OCP) of the system. All measured current in this non-Faradaic potential region is assumed to be associated with double-layer charging. The charging current, i_c , is then measured from CVs at multiple scan rates. The working electrode was held at each potential vertex for 10 s before beginning the next sweep. The double-layer charging current is equal to the product of the scan rate, ν , and the electrochemical double-layer capacitance, C_{DL} , as given by the following equation:

$$i_c = \nu \times C_{DL} \quad (S1)$$

As shown in Figure S12, C_{DL} is 0.95 mF.

The electrochemically active surface area (ECSA) of the membrane is then calculated from the double layer capacitance according to the following equation:

$$ECSA = \frac{C_{DL}}{C_s} \quad (S2)$$

where C_s is the specific capacitance of the sample or the capacitance of an atomically smooth planar surface of the material per unit area under identical electrolyte conditions.

For estimation of the surface area, general specific capacitance of $C_s = 0.04$ mF cm⁻² was used in this work.^{6,7} The mass weight of membrane is 22.5 mg. Thus, the ECSA of the MXene membrane is 10.55 m² g⁻¹.

The potential of zero charge (E_{ZC}) can be used to evaluate the susceptibility of a

material to lose electrons. In particular, a material that exhibits a more positive E_{ZC} value should be less susceptible to loss of electrons.⁸ The E_{ZC} of the MXene membrane was determined using a Bio-Logic potentiostat/galvanostat with EIS capability. Impedance spectra were recorded in the frequency of 1000 Hz, with a modulation amplitude of 1 mV. An initial potential range of 0 to 0.5 V vs Ag/AgCl, with a step size of 10 mV, was performed in order to determine the E_{ZC} . As shown in Figure S13, the E_{ZC} of MXene membrane is approximately 0.14 V.

The LSV curves recorded at nitrate ($850 \text{ mg L}^{-1} \text{ NaNO}_3$) and sulfate ($473.3 \text{ mg L}^{-1} \text{ Na}_2\text{SO}_4$) were used to further identify the peak resulting from the reduction of nitrate (Figure S22). The plot of the cathodic peak current against the scan rate was conducted by the LSV curves (Figure S23). The results suggest that the nitrate adsorption and reduction are controlled by the diffusion process. The cathodic potential was automatically corrected for iR drop in solution by potentiostat (CHI 660E). The iR compensation is 85%.

The EIS Nyquist plots were used to characterize the electron transfer resistance of the membrane. The corresponding figure is provided as Figure S24. The solution resistance of NaNO_3 and Na_2SO_4 are 1286 ohm and 1365 ohm, respectively. The corresponding baseline potential is 0.0235 V.

Section S5. Electrochemical nitrate reduction

Before undertaking the electrochemical nitrate reduction experiments, the rejection property of the MXene membrane was measured with the results presented in Table S1 and S2.

The effect of potential on nitrate reduction is shown in Figure S8 and Figure S9. To explore the impact of sodium intercalation on electrochemical nitrate reduction, we determined the concentration of the products of electrochemical nitrate reduction for different sodium and calcium concentrations. The results suggest that the impact of sodium intercalation and the co-ion effect of Ca^{2+} on nitrate reduction are not significant (Figure S11).

The comparison of nitrate removal using $\text{Ca}(\text{NO}_3)_2$, KNO_3 , and NaNO_3 is

presented in Figure S14. Regardless of the nitrate salt used, the MXene membrane always exhibits high nitrate removal (>75%) and N₂ selectivity (>80%). Therefore, the impact of cation intercalation on the selectivity of the membrane towards nitrate is insignificant in this work.

In the continuous-flow nitrate reduction experiments, the electrode spacing for anode and cathode, anode and reference electrode, cathode and reference electrode is 5.0 cm, 3.5 cm, and 1.5 cm, respectively. The hydraulic retention time of the continuous experiments is 5~25 h at the flux of 20 to 100 L m⁻² h⁻¹ in the device (Figure S15). The residence time of fluid contact with the membrane ranged from 0.36 s to 1.8 s at the flux range of 100~20 L m⁻² h⁻¹.

The pH value increased from 7.8 to 8.3 in the effluent of the continuous flow operation. The corresponding pressure drop across membrane is approximately 22~40 kPa. In the continuous flow experiments, the calculated nitrate diffusion coefficient is $2.04 \times 10^{-9} \text{ m}^2 \text{ s}^{-1}$ (Figure S26), which is higher than the diffusion coefficient in solution in the absence of an applied potential. Therefore, the nitrate transport in the membrane is controlled by the convection.

To further investigate the relationship between yields and nanofluidic channels, we then used the residual nitrate (5.0 mg-N L⁻¹) in batch experiments as the initial concentration in the flow-through mode (Figure S25).

The extent of Ti leaching during the continuous operation was measured with results shown in Figure S27. The net loss of Ti was about 0.23 wt% towards the total weight of Ti.

To investigate the impact of dissolved oxygen on the nitrate electrochemical reduction, the products of the reduction process without Ar purging were quantified. The dissolved oxygen in the applied system is 5.85~6.23 mg L⁻¹. As shown in Figure S35, a slight decline in TN and nitrate removal can be observed in the system without Ar purging, while the reduction selectivity of N₂ was still maintained at over 80%. Thus, the impact of ORR process on the nitrate electrochemical reduction appears to be insignificant.

To further confirm the negligible impact of Cl⁻ on the nitrate reduction, we

analyzed the concentration of free chlorine generated at the anode. Free chlorine concentrations in the reaction system were measured with the N,N-diethyl-p-phenylenediamine (DPD) ferrous titrimetric method and the DPD colorimetric method.⁹ The applied cathode potential is -0.6, -0.7, -0.8, -0.9, and -1.0 V(vs Ag/AgCl). Under this condition, the free chlorine could not be detected in the solution under these conditions (Table S3).

The selectivity of NO_3^- reduction (S_i) was calculated using equation S3:

$$S_i (\%) = n_i \times \left(\frac{c_{p,i}}{c_{f,\text{NO}_3^-} - c_{p,\text{NO}_3^-}} \right) \times 100 \quad (\text{S3})$$

where species i is $\text{NO}_2\text{-N}$, $\text{NH}_3\text{-N}$, $\text{N}_2\text{O-N}$, or $\text{N}_2\text{-N}$, and n_i is the stoichiometric coefficient (*e.g.*, moles of i per mole of NO_3^- reduced). The c_f and c_p values are the feed and permeate concentrations (M) of nitrate, respectively. The apparent N_2 selectivity was calculated assuming that N mass balance is maintained. For analyzing mass balance, the products captured in the electrical double layer were considered by further releasing them under open circuit.

The calculation of C_{gas} (mg $\text{N}_2\text{O-N/L}$) is listed below:

$$C_{\text{gas}} (\text{mg } \text{N}_2\text{O-N/L}) = C_{\text{gas}} (\text{ppmv}) \times 10^{-6} \times \text{gas molar volume}^{-1} (0.041 \text{ mol/L at } 25^\circ\text{C and } 1 \text{ atm}) \times 28 \times 1000$$

The detection limit of C_{gas} (ppmv) is 10 ppmv, and the corresponding detection limit of C_{gas} (mg $\text{N}_2\text{O-N/L}$) is $\sim 0.01 \text{ mg L}^{-1}$.

The detection limit of NH_4^+ , NO_3^- , NO_2^- detected by ion chromatography is 0.01 mg L^{-1} . Thus, the detection limit of obtained N_2 is 0.01 mg L^{-1} .

Hydrogen gas production in the chronoamperometry experiments was detected by gas chromatography with thermal conductivity detector (GC-TCD). Hydrogen concentration was measured by comparing the area under the curve of the hydrogen peak in each chromatogram (1.43 min) against a hydrogen volume fraction calibration curve.

Faradaic efficiency (FE) with regard to N_2 generation was calculated using the following equation S4:

$$FE_{N_2}(\%) = zF \times S_{N_2} \times J \times \left(\frac{c_{f,NO_3^-} - c_{p,NO_3^-}}{j} \right) \times 100 \quad (S4)$$

where z is the moles of electrons transferred per moles of reactant, F is the Faraday constant (96485 C mol⁻¹), J is the membrane flux (L m⁻² s⁻¹), and j is the current density (A m⁻²). The electrical energy per order reduction (E_{EO}), which is a measure of the electric energy (kWh m⁻³) needed to reduce the NO₃⁻ concentration by 1 order of magnitude, was calculated using equation S5:

$$E_{EO} = 10^{-3} \times \left(\frac{V_{cell} I}{q \times \log \left[\frac{c_{f,NO_3^-}}{c_{p,NO_3^-}} \right]} \right) \quad (S5)$$

where V_{cell} is the cell potential (V), I is the current (A), and q is the volumetric permeate flow rate (m³ h⁻¹). The energy consumption (EC_{pump} , kWh m⁻³) for pumping permeate through the cell can be calculated according to equation S6:

$$EC_{pump} = \frac{\Delta P}{3600 \times \eta_{pump}} \quad (S6)$$

where ΔP is the hydraulic pressure drop of the cell (kPa), and η_{pump} is the pump efficiency (65%). The EC_{pump} in our system is 0.009 kWh m⁻³ which is far below that of E_{EO} (0.28 kWh m⁻³). Therefore, E_{EO} can be considered as the total energy cost. Comparison of the MXene membrane with previously reported materials for nitrate reduction is presented in Table S4. In this work, the reduction selectivities of nitrate to NH₄⁺ and NO₂⁻ in the flow-through experiments are 13.7% and 3.5%, respectively.

The N₂ FE of electrochemical nitrate reduction increases with membrane flux, which might be attributed to the sufficient oxygen vacancies on the MXene membrane.

Section S6. DFT calculation.

First-principle calculations were performed by the density functional theory (DFT) using the Vienna Ab-initio Simulation Package (VASP) package. The generalized

gradient approximation (GGA) with the Perdew- Burke-Ernzerhof (PBE) functional was used to describe the electronic exchange and correlation effects. Uniform G-centered k-points meshes with a resolution of $2\pi*0.03 \text{ \AA}^{-1}$ and Methfessel-Paxton electronic smearing were adopted for the integration in the Brillouin zone for geometric optimization. The simulation was run with a cutoff energy of 500 eV throughout the computations. These settings ensure convergence of the total energies to within 1 meV per atom. Structure relaxation in the models proceeded with all forces on atoms less than 1 meV \AA^{-1} and the total stress tensor was within 0.01 GPa of the target value.

The activation energies of the nitrate electrochemical reduction are calculated by the transition state of an elementary reaction step. The transition state of an elementary reaction step was located by the nudged elastic band (NEB) method. In the NEB method, the path between the reactant(s) and product(s) was discretized into a series of five structural images. The intermediate images were relaxed until the perpendicular forces were smaller than 0.02 eV/\AA . The corresponding activation energies are presented in Figure S29.

Proposed corresponding reaction pathway and free energy of nitrate electrochemical reduction on perfect MXene sites is illustrated in Figure S16 and Figure S31. Predicted deformation charge densities of $*\text{NO}_3$ on the defect MXene and defect-free MXene are presented in Figure S32. Calculated adsorption energies of HER process on the surface of MXene is presented in Figure S33. Calculated adsorption energies of H_2 on the surface of MXene is presented in Figure S34.

The adsorption free energy involves adsorbed species including $*\text{NO}_3$, $*\text{NO}_2$, $*\text{NO}$, $*\text{N}$, $*\text{NH}_3$ and $*\text{N}_2\text{O}$ can be expressed by equation S7:

$$\Delta G = \Delta E_{\text{ads}} + \Delta E_{\text{ZPE}} - T\Delta S + \Delta G_{\text{u}} \quad (\text{S7})$$

where ΔE_{ads} is the adsorption energy change of adsorbates, E_{ZPE} is the zero energy calculated from the vibrational frequencies, ΔS is the entropy change, and T is the system temperature (298.15 K, in this work). $\Delta G_{\text{u}} = -eU$ (U is the potential measured against normal hydrogen electrode).

Supplementary Figures and Tables

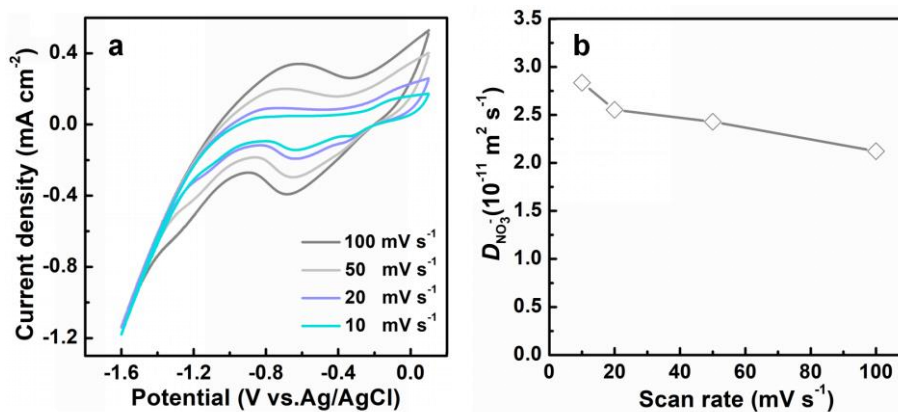


Figure S1. (a) Cyclic voltammograms of Cu electrode. (b) Diffusion coefficient under different scan rates.

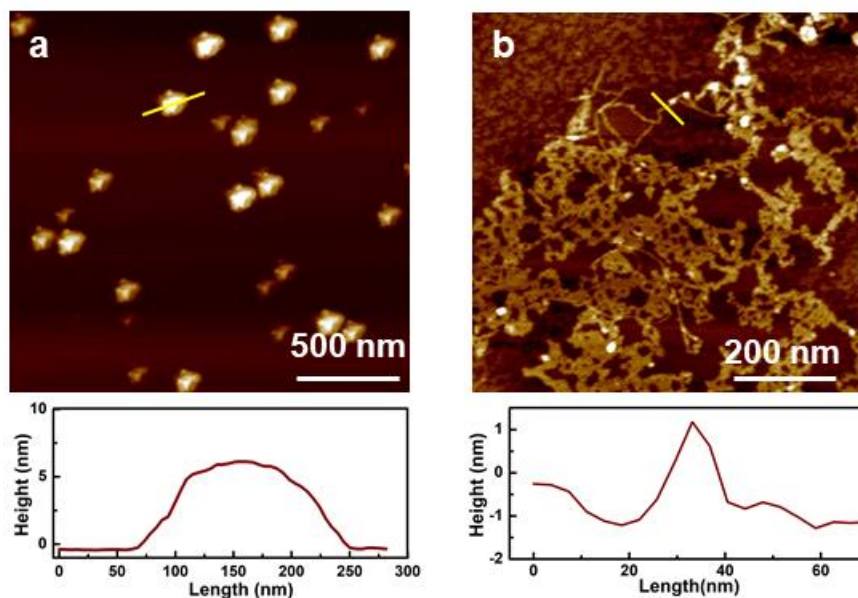


Figure S2. AFM height images and the corresponding height profile along the crossed lines for Ti₃C₂T_x MXene. (a) Ti₃C₂T_x MXene nanosheets, and (b) is ANF dispersion.

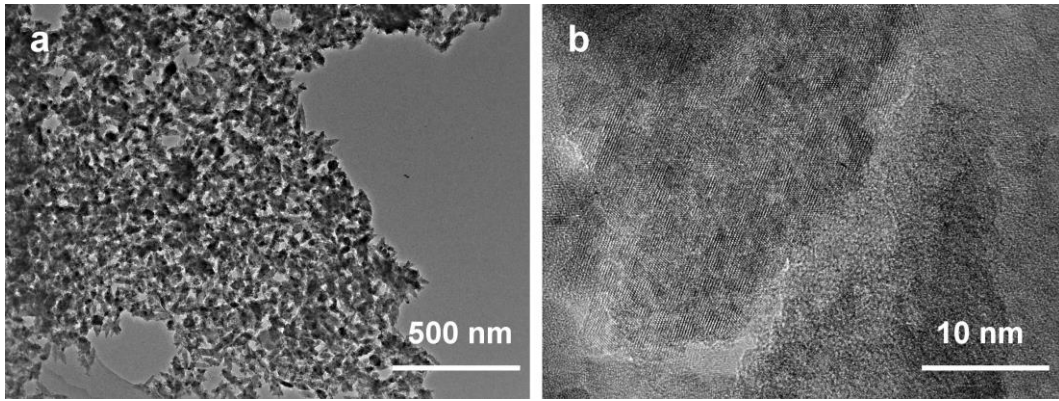


Figure S3. TEM images of MXene nanosheets (a) at 500 nm scale and (b) at 10 nm scale.

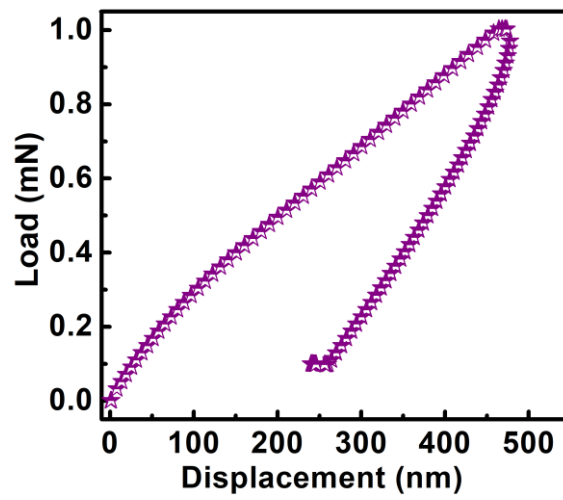


Figure S4. Plots of displacement vs. load of the MXene membrane.

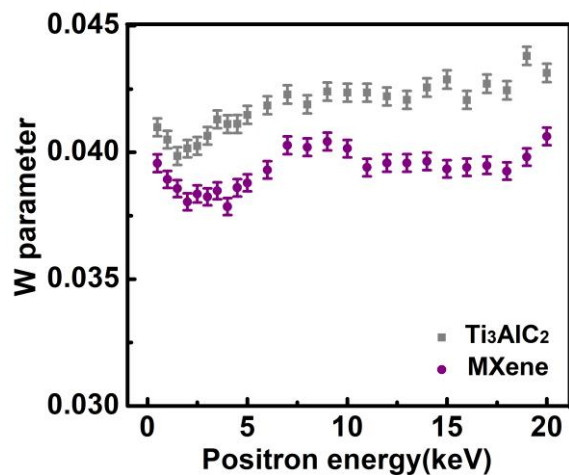


Figure S5. Doppler broadening W parameter of $\text{Ti}_3\text{C}_2\text{T}_x$ MXene and Ti_3AlC_2 as a function of incident energy.

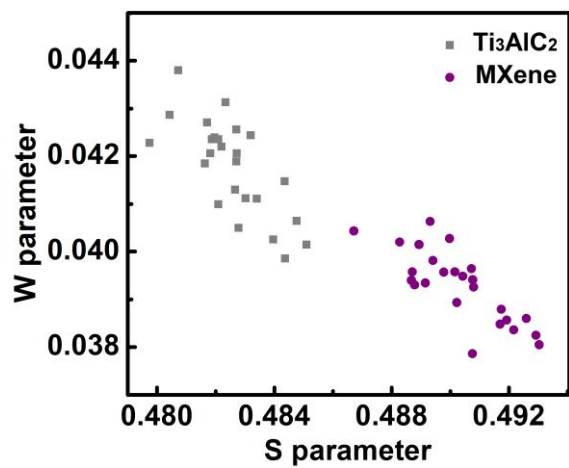


Figure S6. Doppler broadening W-S parameters of $\text{Ti}_3\text{C}_2\text{T}_x$ MXene and Ti_3AlC_2 as a function of incident energy.

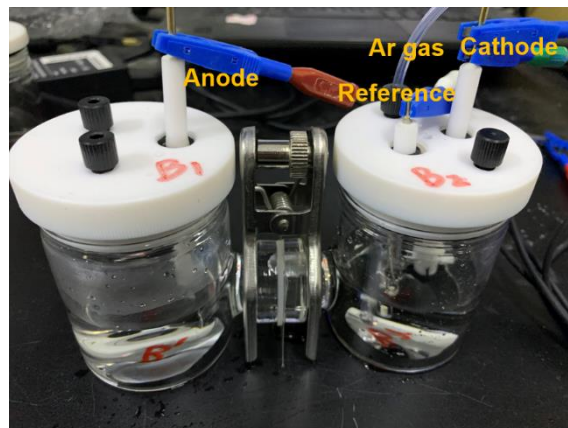


Figure S7. Schematic illustration of the H-shaped electrochemical reaction cell.

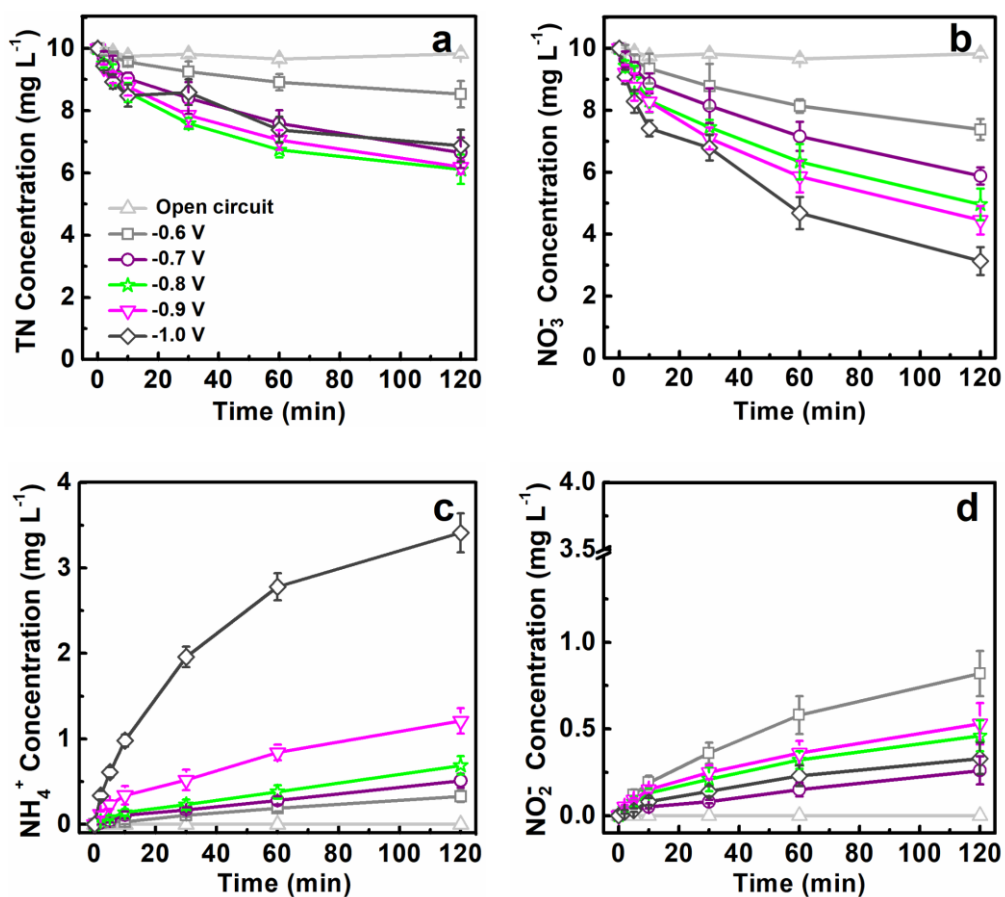


Figure S8. Effects of variation in potential on (a) TN removal, (b) NO₃-N removal, (c) NH₃-N generation, and (d) NO₂-N generation. Working conditions: [NaNO₃] = 60.7 mg L⁻¹, total solution volume = 50 mL, pH 6.6, *T* = 25 °C.

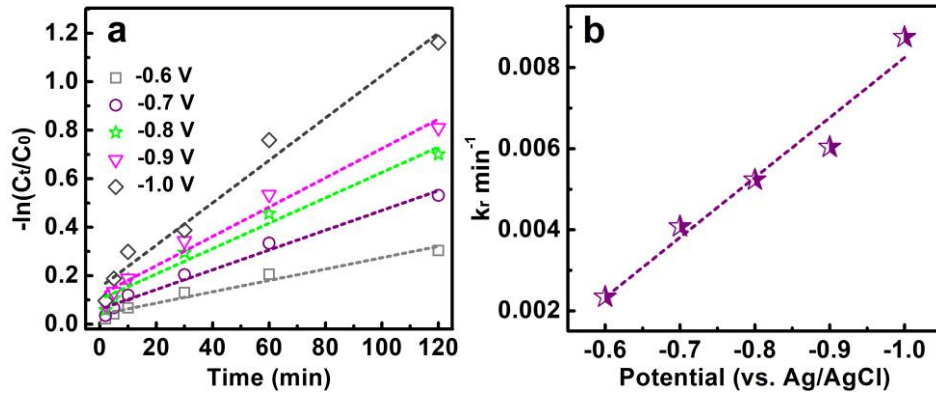


Figure S9. (a) Kinetics of the electrochemical NO_3^- reduction assuming a pseudo first-order kinetics. (b) Effect of potential on reaction kinetics.

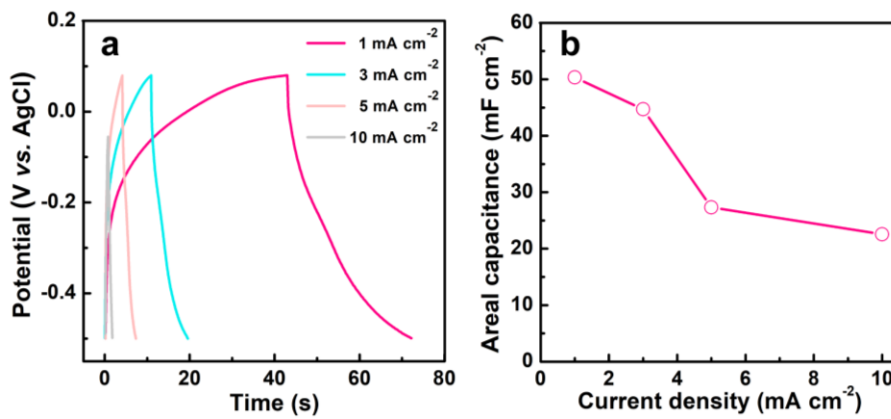


Figure S10. (a) The galvanostatic charge-discharge curves of the MXene membrane. (b) Areal capacitance at various specific currents.

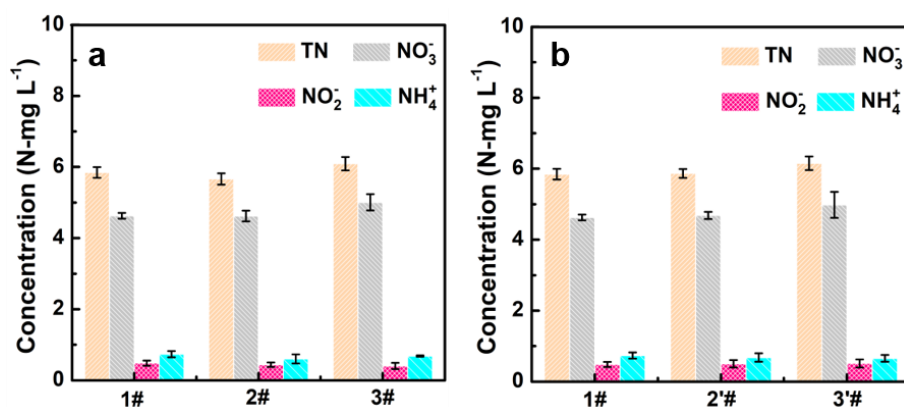


Figure S11. The products of nitrate reduction under different Na⁺ and Ca²⁺ concentration. (a) Na⁺ and (b) Ca²⁺. Experimental conditions: (1#) [NaNO₃] = 60.7 mg L⁻¹, [NaHCO₃] = 200 mg L⁻¹, [Na₂SO₄] = 200 mg L⁻¹, [NaCl] = 100 mg L⁻¹. (2#) [NaNO₃] = 60.7 mg L⁻¹, [NaHCO₃] = 200 mg L⁻¹, [Na₂SO₄] = 735.6 mg L⁻¹, [NaCl] = 100 mg L⁻¹. (3#) [NaNO₃] = 60.7 mg L⁻¹, [NaHCO₃] = 200 mg L⁻¹, [Na₂SO₄] = 1271.2 mg L⁻¹, [NaCl] = 100 mg L⁻¹. (2'#) [NaNO₃] = 60.7 mg L⁻¹, [NaHCO₃] = 200 mg L⁻¹, [Na₂SO₄] = 200 mg L⁻¹, [NaCl] = 100 mg L⁻¹, [CaCl₂] = 111 mg L⁻¹. (3'#) [NaNO₃] = 60.7 mg L⁻¹, [NaHCO₃] = 200 mg L⁻¹, [Na₂SO₄] = 200 mg L⁻¹, [NaCl] = 100 mg L⁻¹, [CaCl₂] = 222 mg L⁻¹.

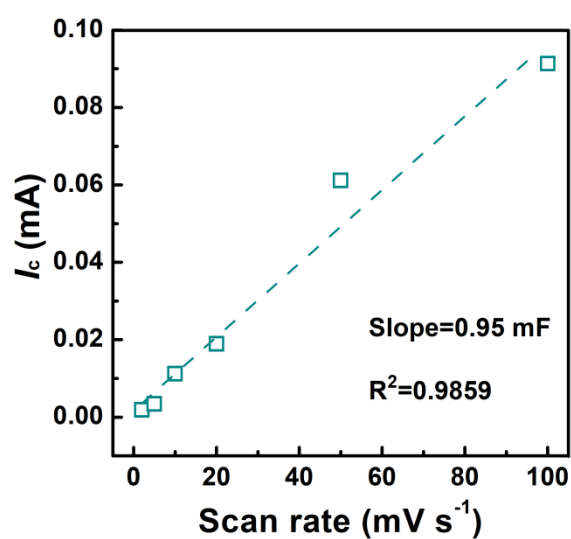


Figure S12. Double-layer capacitance measurements for determining electrochemically active surface area for the MXene membrane.

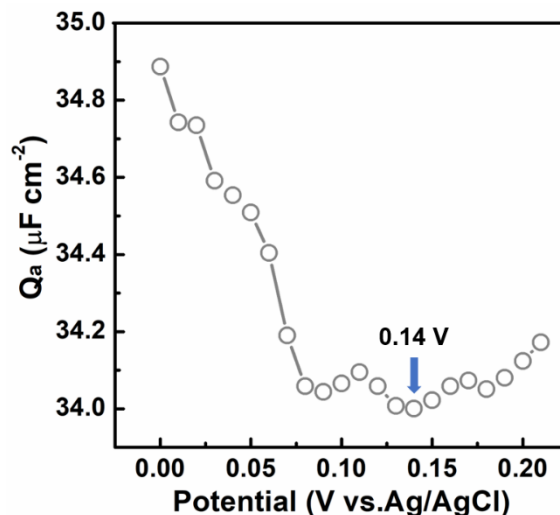


Figure S13. Electrochemical impedance spectroscopy of MXene membrane at 10 mV intervals in 100 mM NaNO₃ at pH 6.8. The resulting Nyquist plots were modeled as Rs-(C-Rp) circuits. The calculated capacitance values (dots) for each sample are shown here. The minimum value of each curve represents the E_{ZC}. The magnitude of the capacitance is representative of the surface area of the sample

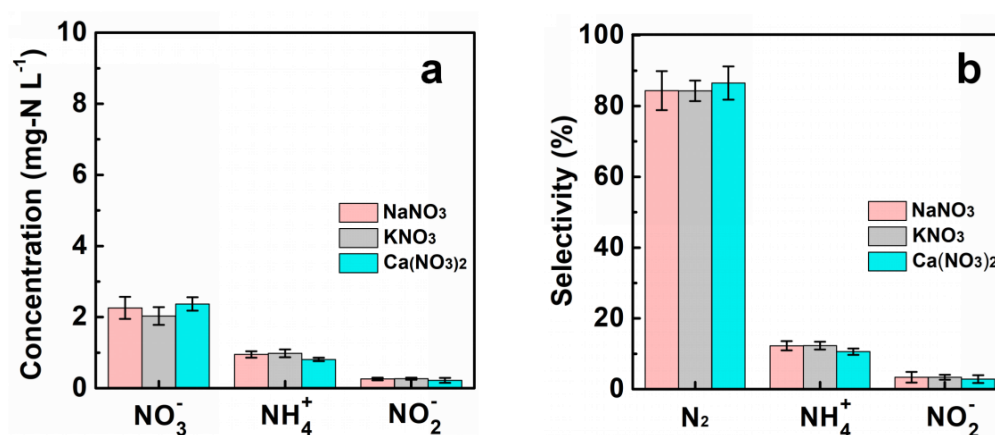


Figure S14. (a) The concentration of NO₃⁻, NH₄⁺, and NO₂⁻ in the effluent of the continuous-flow experiment. The initial concentration of NaNO₃, KNO₃, and Ca(NO₃)₂ are 0.71 mM (10 mg-N L⁻¹). The applied potential of cathode is -0.8 V (vs Ag/AgCl) and the membrane flux is 100 L m⁻² h⁻¹. (b) The selectivity of products (N₂, NH₄⁺, and NO₂⁻) in the nitrate reduction process.

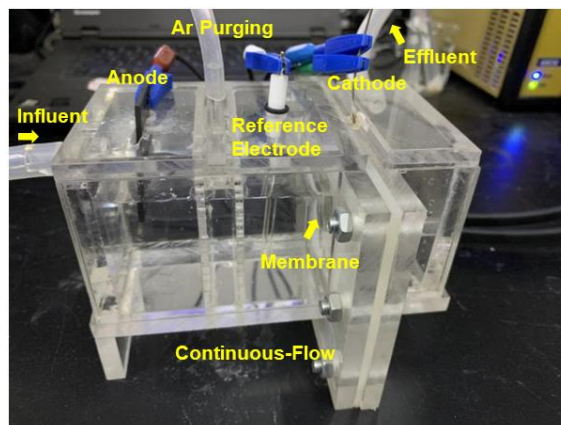


Figure S15. Photograph of the continuous-flow reactor with notations.

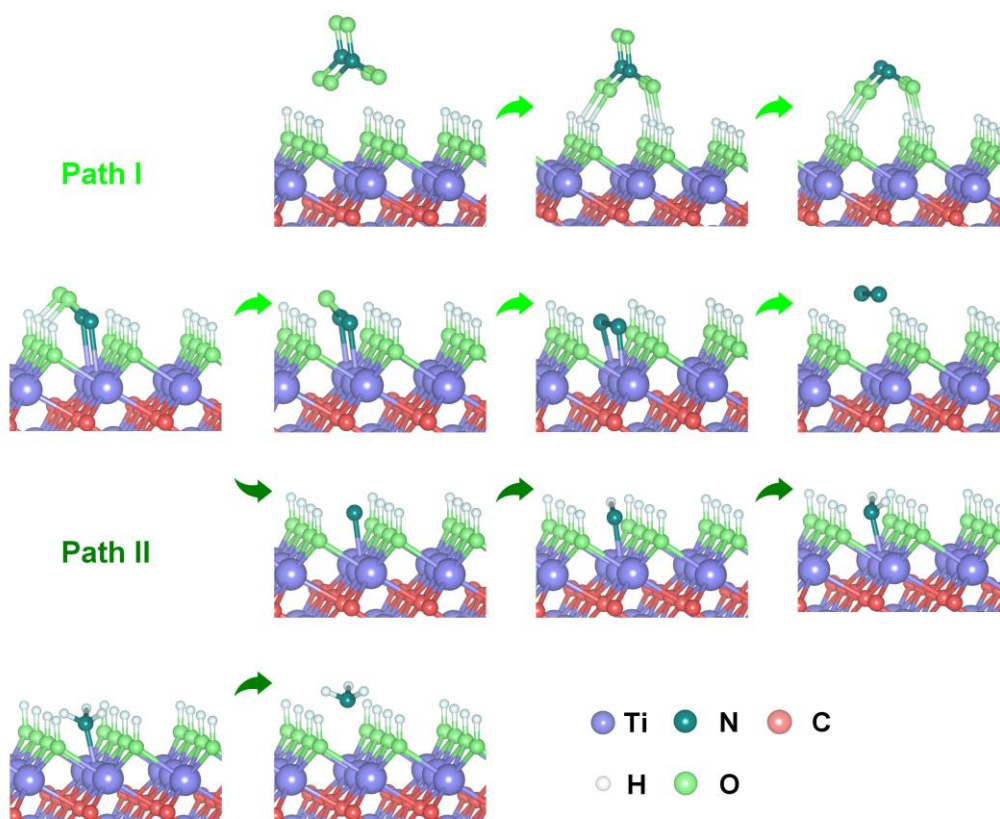


Figure S16. Proposed reaction pathway of nitrate electrochemical reduction on the defect-free MXene sites.

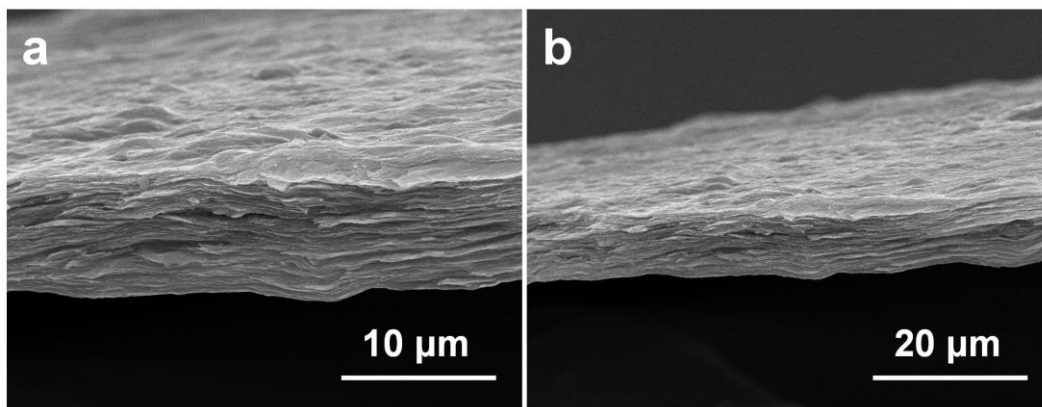


Figure S17. SEM images of cross-section of the MXene membrane. (a) at 10 μm scale and (b) at 20 μm scale.

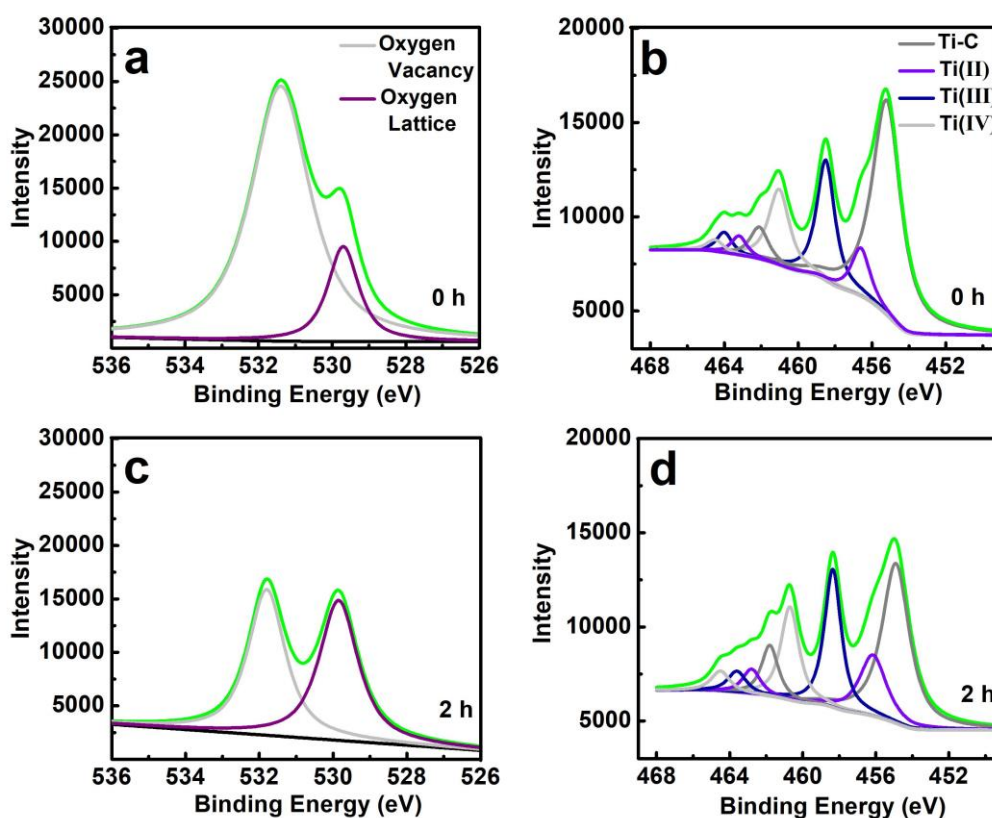


Figure S18. X-ray photoelectron spectroscopy (XPS) of (a) O1s and (b) Ti 2p at t = 0 h and (c) O1s and (d) Ti 2p at t = 2 h after electrochemical nitrate reduction. The intensity is relative intensity. The relative heights are expected to be more important (*i.e.*, the relative gain in lattice oxygen might only be due to loss of oxygen vacancies by reduction) because the continuous Ar purging should largely exclude the influence of oxygen coming from the anode upstream. Experimental conditions: [NaNO₃] = 60.7 mg L⁻¹, pH 6.6, T = 25 °C, applied potential = -0.8 V vs Ag/AgCl.

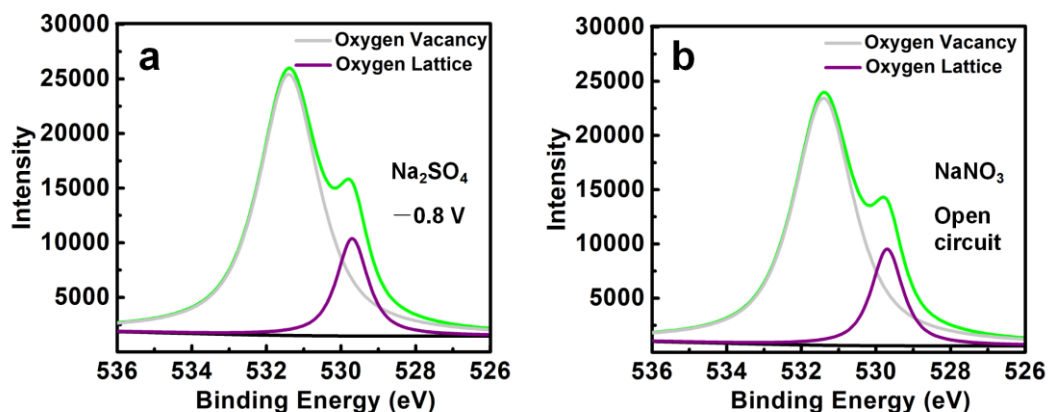


Figure S19. O 1s spectra of the as-prepared MXene membrane. (a) Spectra obtained in Na_2SO_4 solution at -0.8 V (vs Ag/AgCl), and (b) Spectra obtained in NaNO_3 solution at open circuit. The operation period is 24 h.

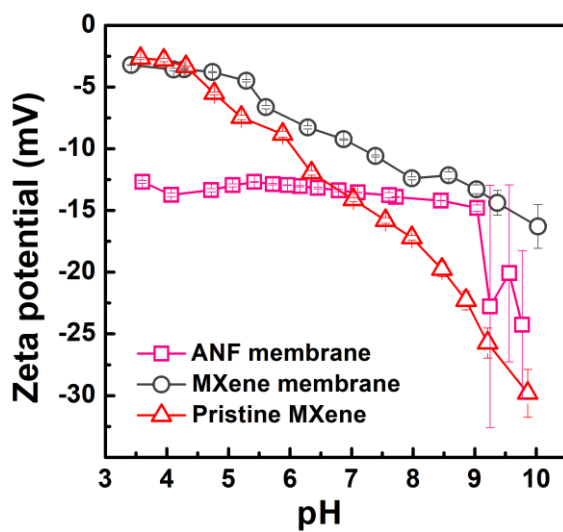


Figure S20. Zeta potential measurements of pristine MXene membrane, MXene membrane, and ANF membrane. For the sample of pristine MXene and ANF membranes, they were obtained by the simple vacuum filtration of MXene and ANF solution on the anodized aluminum filter, respectively.

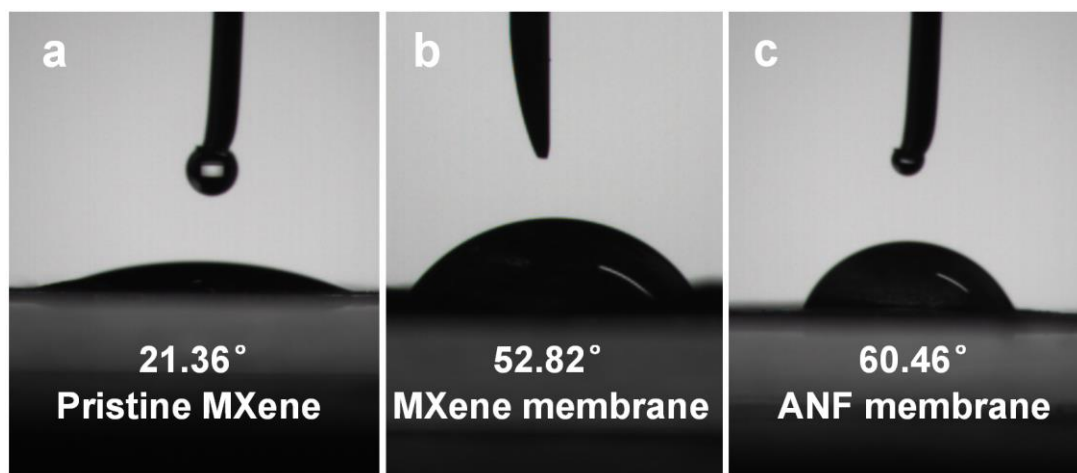


Figure S21. Water contact angles of (a) pristine MXene membrane, (b) MXene membrane, and (c) ANF membrane. For the sample of pristine MXene and ANF membranes, they were obtained by the vacuum filtration of MXene and ANF solution on the anodized aluminum filter, respectively.

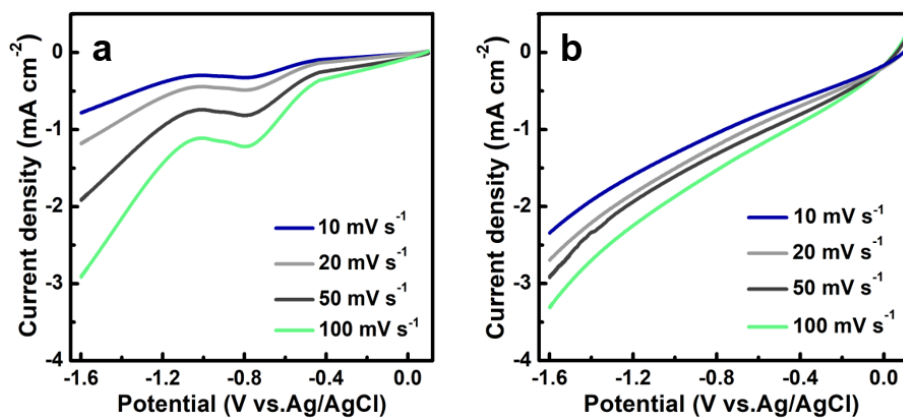


Figure S22. Electrochemical performance of the MXene membrane and product analysis during electrochemical nitrate reduction. Linear sweep voltammograms of the MXene membrane in (a) NaNO_3 (850.0 mg L^{-1}) and (b) Na_2SO_4 (473.3 mg L^{-1}) solutions with the corresponding scan rates from 10 to 100 mV s^{-1} .

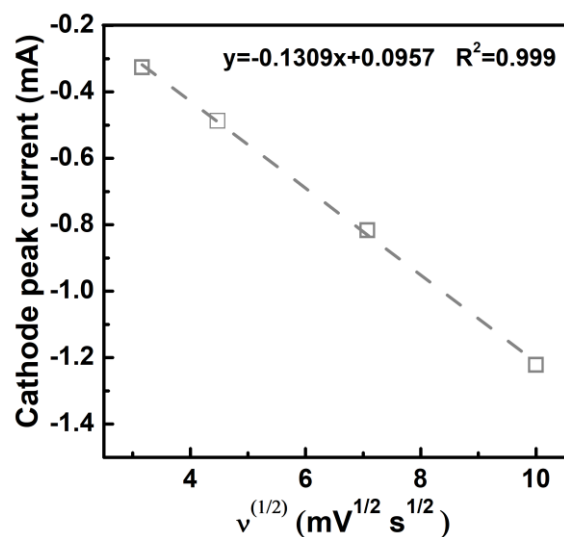


Figure S23. Peak heights on square root of scan rate measured by LSV at the MXene membrane. The detected solution is NaNO₃.

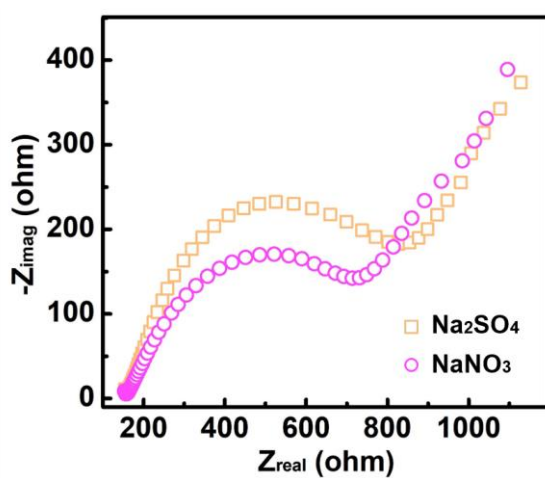


Figure S24. EIS Nyquist plots of the MXene cathodes in different electrolyte solutions with an applied impedance amplitude of 10 mV over a frequency range from 10⁵ to 10⁻² Hz. The baseline potential is 0.0235 V. The concentrations of Na₂SO₄ and NaNO₃ are 50.7 mg L⁻¹ and 60.7 mg L⁻¹, respectively.

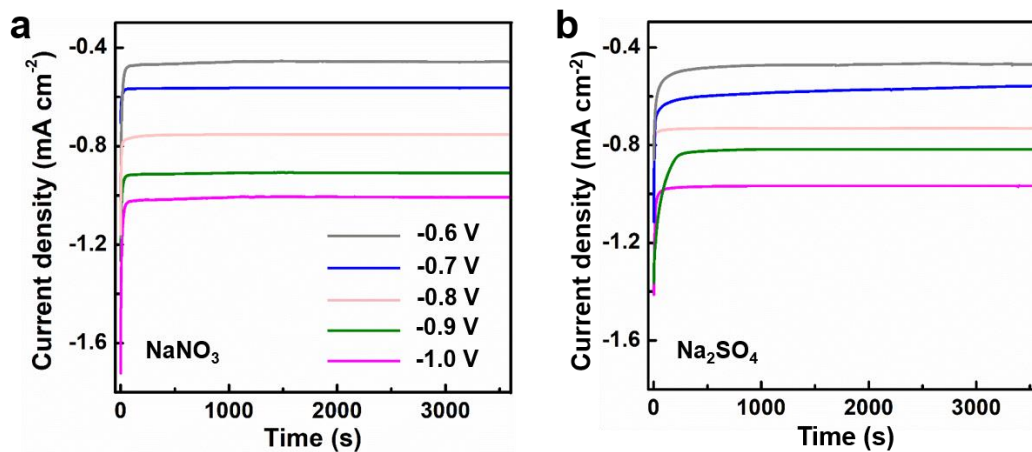


Figure S25. Chronoamperometry experiments of MXene membrane at different potentials (vs Ag/AgCl) in (a) NaNO₃ solution and (b) Na₂SO₄ solution.

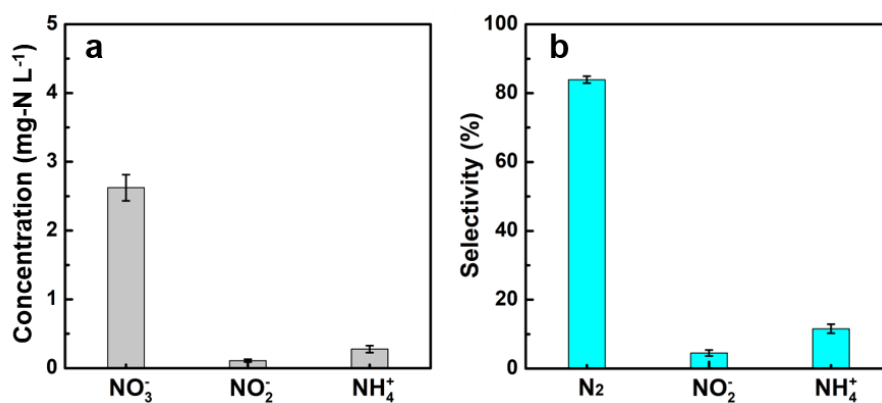


Figure S26. Electrochemical reduction of low concentration nitrate under the flow-through filtration. Experimental condition: [NaNO₃] = 30.4 mg L⁻¹.

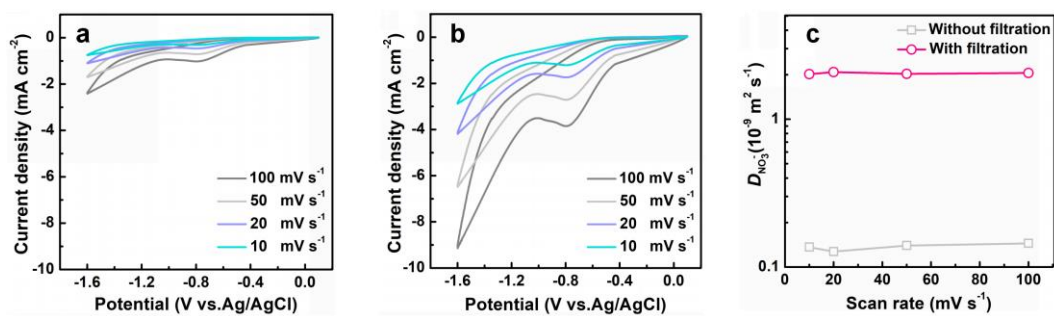


Figure S27. Cyclic voltammograms of (a) no filtration and (b) with filtration (in a flow-through mode, $100 \text{ L}^{-1} \text{ m}^2 \text{ h}^{-1}$). (c) Diffusion coefficients of nitrate with and without filtration ($2.04 \times 10^{-9} \text{ m}^2 \text{ s}^{-1}$ and $0.14 \times 10^{-9} \text{ m}^2 \text{ s}^{-1}$).

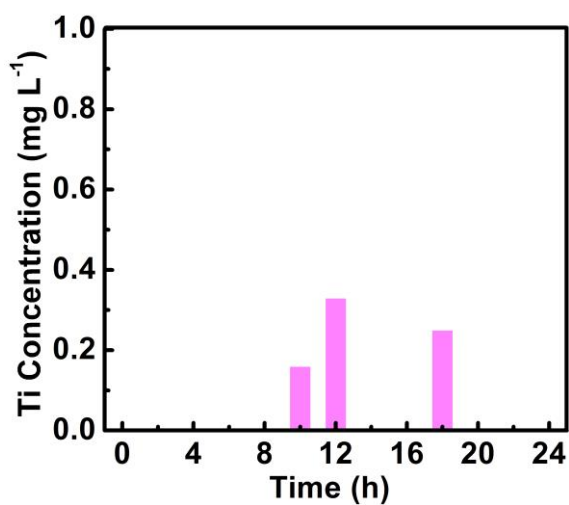


Figure S28. Leaching of Ti as a function of time for the MXene membrane at a permeate flux of $100 \text{ L m}^{-2} \text{ h}^{-1}$. The weight of the membrane is $40\text{--}60 \text{ g m}^{-2}$. The net loss of Ti was about 0.23 wt% towards the total weight of Ti.

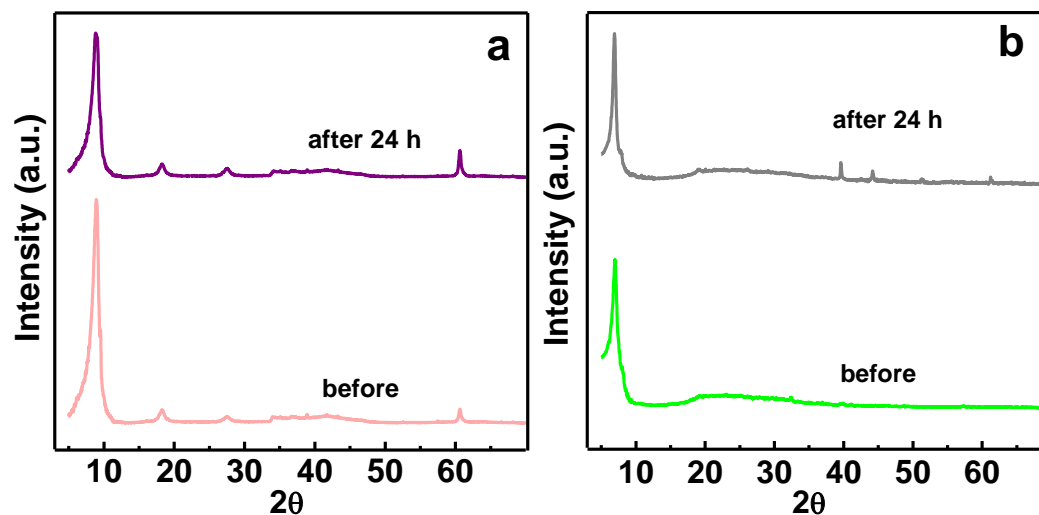


Figure S29. XRD patterns of the MXene membrane before and after the 24-h electrochemical NO_3^- reduction experiment. (a) Sample under dry condition, (b) sample under hydrated condition.

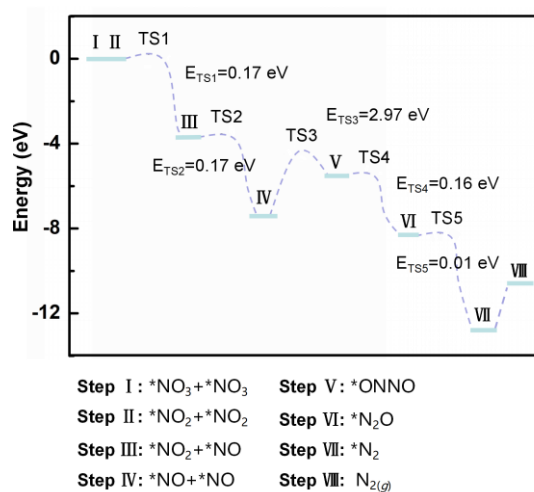


Figure S30. Calculated transition barrier energy profiles for the nitrate electrochemical reduction on the $\text{Ti}_3\text{C}_2\text{T}_x$ MXene.

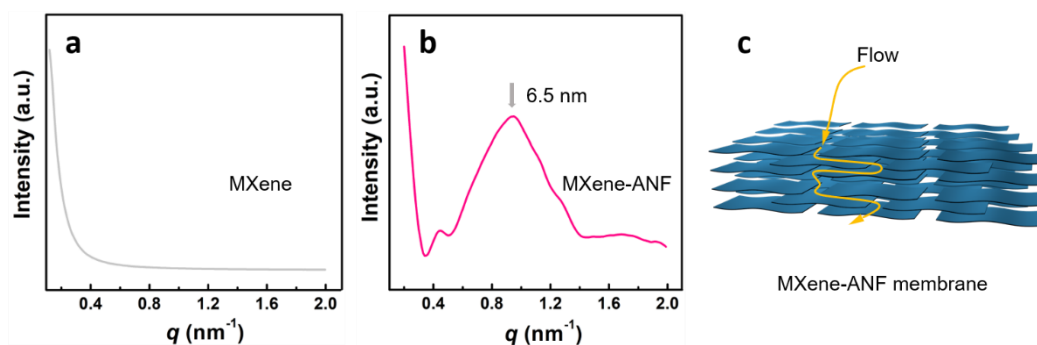


Figure S31. (a) SAXS profiles of the MXene membrane without ANF and (b) intercalated by ANF. (c) Schematic of the interior structure of the MXene/ANF composite membrane. The MXene membrane without ANF is obtained by vacuum filtration of MXene suspension on the anodized aluminum filter substrate (0.2 μm).

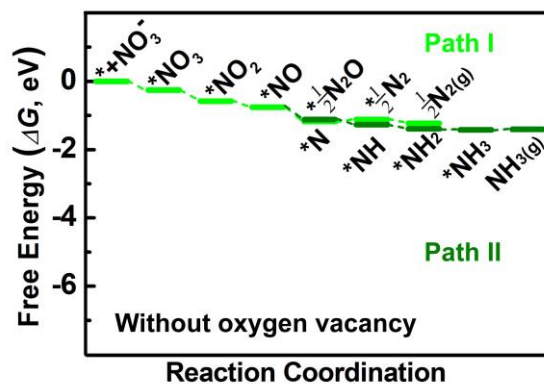


Figure S32. Calculated free energy of the proposed reaction pathways (Path I: Nitrate to $\text{N}_2(\text{g})$ and Path II: Nitrate to $\text{NH}_3(\text{g})$) for nitrate reduction on the defect-free MXene nanosheets.

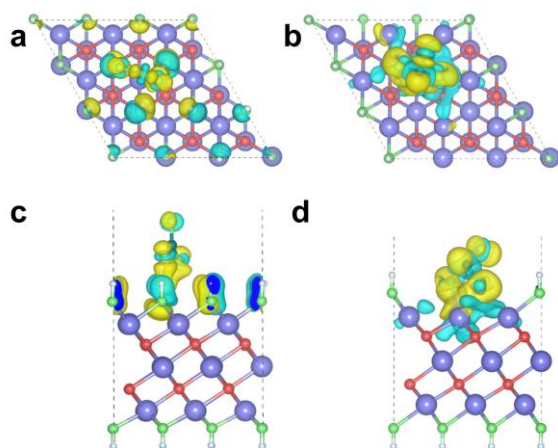


Figure S33. The deformation charge density of $*\text{NO}_3$. Top view: (a) is the defect-free MXene, (b) is the MXene with oxygen vacancies. Side view: (c) is the defect-free MXene, (d) is the MXene with oxygen vacancies. The cyan region is electron deficient area.

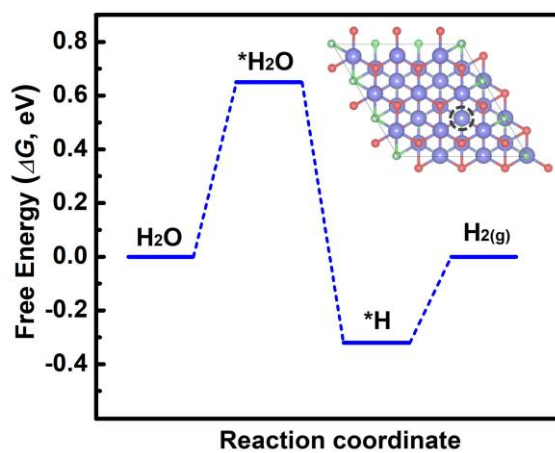


Figure S34. Calculated free energies of HER process on the surface of the MXene with oxygen vacancies (with defects).

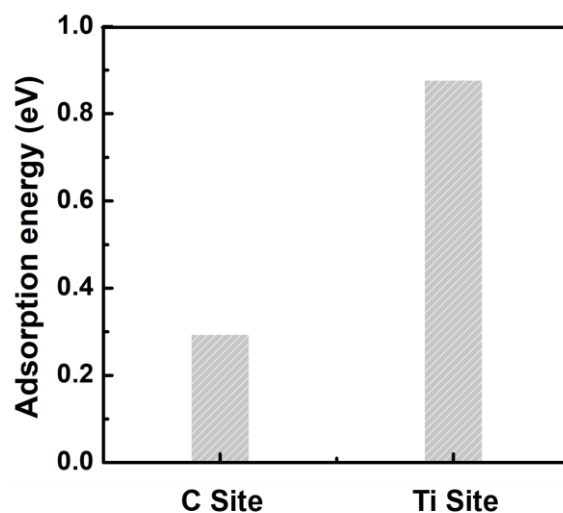


Figure S35. Calculated adsorption energies of H_2 on the C and Ti sites of the MXene with oxygen vacancies (with defects).

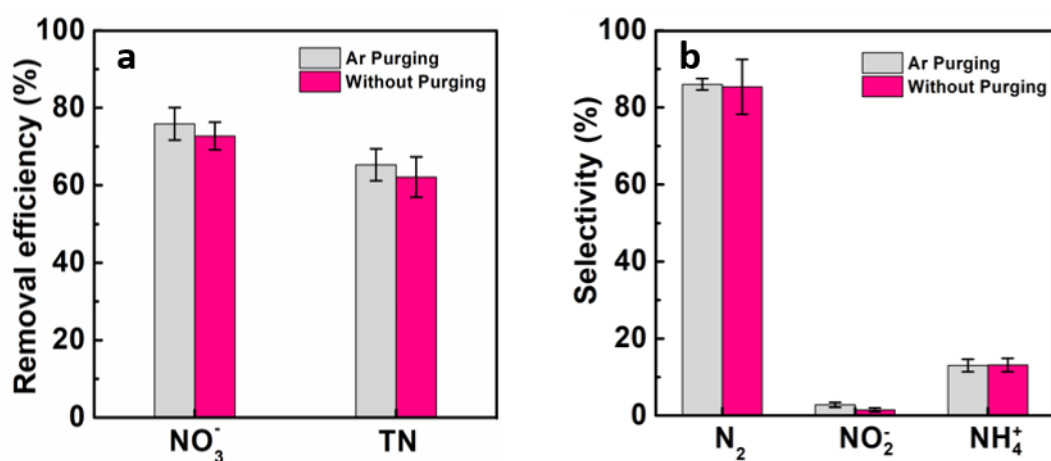


Figure S36. Removal efficiency and electrochemical products under different operating conditions (Ar purging and without purging). The dissolved oxygen concentrations in the applied system with and without Ar purging are $0.32 - 0.56 \text{ mg L}^{-1}$ and $5.85 - 6.23 \text{ mg L}^{-1}$, respectively. Experimental conditions: $[NaNO_3] = 60.7 \text{ mg L}^{-1}$, $[NaHCO_3] = 200 \text{ mg L}^{-1}$, $[Na_2SO_4] = 200 \text{ mg L}^{-1}$, $[NaCl] = 100 \text{ mg L}^{-1}$, pH 7.6, $T = 25 \text{ }^\circ\text{C}$, applied cathode potential = $-0.8 \text{ V (vs Ag/AgCl)}$, and membrane flux is $100 \text{ L m}^{-2} \text{ h}^{-1}$.

Table S1. Polyethylene glycol (PEG) rejection by the MXene membrane for various PEG concentrations. The rejection is calculated using TOC values.

PEG (mg L ⁻¹)	5	10	50	100
R(PEG-10 kDa) (%)	97.6 ± 1.4	~100	~100	~100

Table S2. Nitrate (60.7 mg L⁻¹ NaNO₃) rejection of the MXene membrane as function of the permeate flux.

Membrane flux (L m ⁻² h ⁻¹)	20	40	60	80	100
Nitrate rejection (%)	2.3 ± 0.4	1.8 ± 0.2	0.7 ± 0.5	1.4 ± 0.3	2.2 ± 0.7

Table S3. Concentrations of free chlorine at different applied potentials. The reaction time is 1 h.

Potential (V vs Ag/AgCl)	-0.6	-0.7	-0.8	-0.9	-1.0
Free chlorine	ND	ND	ND	ND	ND

ND represents not detectable. Experimental conditions: [NaHCO₃] = 200 mg L⁻¹, [Na₂SO₄] = 200 mg L⁻¹, [NaCl] = 100 mg L⁻¹, pH= 7.7, T = 25 °C.

Table S4. Comparison of the 2D-MXene electrochemical NO_3^- reduction performance to that using a number of previously reported materials. $R(\text{NO}_3^-)$, $R(\text{TN})$, E_{EO} and FE are removal efficiencies of NO_3^- , electrical energy consumption per order metric, and Faradaic efficiencies for NO_3^- reduction to N_2 , respectively.

Cathode	$R(\text{NO}_3^-)$ (%)	$R(\text{TN})$ (%)	N_2 Selectivity (%)	E_{EO} (kWh/m ³)	FE N_2 (%)	Cell voltage (V)	Current (mA)	Initial concentration C_0 (mg/L)	Volume (mL)	Time	Nitrate removal rate (g m ⁻² h ⁻¹)	Ref
2D-MXene membrane	73	60	82.8	0.27	73.59	1.98	4	10-N	100	2 h	0.74	This work
Pd-Cu-PPy	96	~96	~100	5.72	21	3.2	50	50-N	30	1.5 h	1.37	10
Pd-Cu/REMs	43	12	29	1.10	29	5	~	14-N	100	20 min	18.06	11
Pd-Sn/AC	90	82	90.8	0.99	28.86	1.5	30	24.6-N	60	80 min	~	12
Sn-Pd-SS	95	77	81	0.53	~	1.86	40	112-N	500	5 h	8.87	13
Co ₃ O ₄ -TiO ₂ /Ti	89	27	30	6.78	1.15	2.6	125	50-N	100	2 h	1.78	14
GO-Ti	95	0.86	0.91	26.87	5.43	2.2	760	100-N	100	2 h	2.38	15
Fe	91	63	68.8	37.18	2.06	2.7	360	50-N	100	4 h	0.47	16
Cu-Ni	87	2	2.48	51.74	1.48	2.4	237	1400-N	100	8 h	50.75	17
Fe(20%)-N-C	83	21	25	291.91	0.11	2.6	360	50-N	100	24 h	0.19	18
Sn	99.5	88.6	89	~	~	2.9	~	700-N	~	2 h	1.73	19
Cu ₉₀ Ni ₁₀	92	92	100	~	~	2.6	~	140-N	200	24 h	~	20
P doped-Co ₃ O ₄	91.8	91.8	100	~	~	2.6	~	50-N	70	2 h	~	21

Table S5. The yield rate and Faradaic efficiencies (FE) for H₂ in the electrochemical nitrate reduction (in the presence of nitrate) at different potentials.

Cathode potential (V vs. Ag/AgCl)	-0.6 V	-0.7 V	-0.8 V	-0.9 V	-1.0 V
Yield rate (mg h ⁻¹ m ⁻²)	0	0	0	0	20.1±0.5
FE (%)	0	0	0	0	9.1±0.2

Table S6. The yield rate and Faradaic efficiencies (FE) for H₂ generation in Na₂SO₄ solution (in the absence of nitrate) at different potentials.

Cathode potential (V vs. Ag/AgCl)	-0.6 V	-0.7 V	-0.8 V	-0.9 V	-1.0 V
Yield rate (mg h ⁻¹ m ⁻²)	0	0	0	0	26.4±2.3
FE (%)	0	0	0	0	11.2±1.0

Supplementary References

- [1] Libansky, M.; Zima, J.; Barek, J.; Reznickova, A.; Svorcik, V.; Dejmekova, H. Basic Electrochemical Properties of Sputtered Gold Film Electrodes. *Electrochimica Acta* 2017, 251, 452–460.
- [2] Bao, J.-J.; Zou, B.-K.; Cheng, Q.; Huang, Y.-P.; Wu, F.; Xu, G.-W.; Chen, C.-H. Flexible and Free-Standing LiFePO₄/TPU/SP Cathode Membrane Prepared via Phase Separation Process for Lithium Ion Batteries. *J. Membr. Sci.* 2017, 541, 633–640.
- [3] Lu, X.; Gabinet, U. R.; Ritt, C. L.; Feng, X.; Deshmukh, A.; Kawabata, K.; Kaneda, M.; Hashmi, S. M.; Osuji, C. O.; Elimelech, M. Relating Selectivity and Separation Performance of Lamellar Two-Dimensional Molybdenum Disulfide (MoS₂) Membranes to Nanosheet Stacking Behavior. *Environ. Sci. Technol.* 2020, 54 (15), 9640–9651.
- [4] Dou, Z.; Zhou, Y.; Shen, Y.; Xu, X.; Hu, S.; Yang, L.; Qin, Z. Realizing Ultrahigh Areal Capacitance and Cycle Stability of Polyaniline Nanofiber Network Grown on Graphene-Modified Carbon Cloth with the Addition of Trivalent Iron Ions in Electrolyte. *Electrochimica Acta* 2020, 351, 136448.
- [5] Xie, W.; Wang, Y.; Zhou, J.; Zhang, M.; Yu, J.; Zhu, C.; Xu, J. MOF-Derived CoFe₂O₄ Nanorods Anchored in MXene Nanosheets for All Pseudocapacitive Flexible Supercapacitors with Superior Energy Storage. *Appl. Surf. Sci.* 2020, 534, 147584. <https://doi.org/10.1016/j.apsusc.2020.147584>.
- [6] McCrory, C. C. L.; Jung, S.; Ferrer, I. M.; Chatman, S. M.; Peters, J. C.; Jaramillo, T. F. Benchmarking Hydrogen Evolving Reaction and Oxygen Evolving Reaction Electrocatalysts for Solar Water Splitting Devices. *J. Am. Chem. Soc.* 2015, 137 (13), 4347-4357.
- [7] Cossar, E.; Houache, M. S. E.; Zhang, Z.; Baranova, E. A. Comparison of Electrochemical Active Surface Area Methods for Various Nickel Nanostructures. *J. Electroanal. Chem.* 2020, 870, 114246.
- [8] Finke, C. E.; Omelchenko, S. T.; Jasper, J. T.; Lichterman, M. F.; Read, C. G.; Lewis, N. S.; Hoffmann, M. R. Enhancing the Activity of Oxygen-Evolution and Chlorine-Evolution Electrocatalysts by Atomic Layer Deposition of TiO₂. *Energy Environ. Sci.* 2019, 12 (1), 358–365. <https://doi.org/10.1039/C8EE02351D>.

- [9] Ye, Y.; Chang, P. H.; Hartert, J.; Wigginton, K. R. Reactivity of Enveloped Virus Genome, Proteins, and Lipids with Free Chlorine and UV₂₅₄. *Environ. Sci. Technol.* 52 (14), 7698-7708 (2018).
- [10] Chen, C. et al. Combination of Pd-Cu Catalysis and Electrolytic H₂ Evolution for Selective Nitrate Reduction Using Protonated Polypyrrole as a Cathode. *Environ. Sci. Technol.* 53, 13868-13877 (2019).
- [11] Gayen, P. et al. Electrocatalytic Reduction of Nitrate using Magnéli Phase TiO₂ Reactive Electrochemical Membranes Doped with Pd-based Catalysts. *Environ. Sci. Technol.* 52, 9370-9379 (2018).
- [12] Lan, H. et al. Efficient Nitrate Reduction in a Fluidized Electrochemical Reactor Promoted by Pd-Sn/AC Particles. *Catal. Lett.* 146, 91-99 (2015).
- [13] Su, J.F. et al. Mode of electrochemical deposition on the structure and morphology of bimetallic electrodes and its effect on nitrate reduction toward nitrogen selectivity. *Appl. Catal. B: Environ.* 257, 117909 (2019).
- [14] Gao, J. et al. Non-precious Co₃O₄-TiO₂/Ti cathode based electrocatalytic nitrate reduction: Preparation, performance and mechanism. *Appl. Catal. B: Environ.* 254, 391-402 (2019).
- [15] Ma, X. et al. A graphene oxide nanosheet-modified Ti nanocomposite electrode with enhanced electrochemical property and stability for nitrate reduction. *Chem. Eng. J.* 348, 171-179 (2018).
- [16] Li, W. et al. Electrochemical Reduction of High-Concentrated Nitrate Using Ti/TiO₂ Nanotube Array Anode and Fe Cathode in Dual-Chamber Cell. *Catal. Lett.* 146, 2585-2595 (2016).
- [17] Mattarozzi, L. et al. Hydrogen evolution assisted electrodeposition of porous Cu-Ni alloy electrodes and their use for nitrate reduction in alkali. *Electrochim. Acta.* 140, 337-344 (2014).
- [18] Duan, W. et al. Highly active and durable carbon electrocatalyst for nitrate reduction reaction. *Water Res.* 161, 126-135 (2019).
- [19] Katsounaros, I.; Ipsakis, D.; Polatides, C.; Kyriacou, G. Efficient Electrochemical Reduction of Nitrate to Nitrogen on Tin Cathode at Very High Cathodic Potentials. *Electrochimica Acta.* 52 (3), 1329-1338 (2006).
- [20] Reyter, D.; Bélanger, D.; Roué, L. Optimization of the Cathode Material for Nitrate Removal

by a Paired Electrolysis Process. *J. Hazard. Mater.* 192 (2), 507-513 (2011).

- [21] Gao, J.; Jiang, B.; Ni, C.; Qi, Y.; Bi, X. Enhanced Reduction of Nitrate by Noble Metal-Free Electrocatalysis on P Doped Three-Dimensional Co_3O_4 Cathode: Mechanism Exploration from Both Experimental and DFT Studies. *Chem. Eng. J.* 382, 123034 (2020).